

Use of streamflow indices to identify the catchment drivers of hydrograph

Jeenu Mathai¹ and Pradeep P. Mujumdar^{1,2}

¹Department of Civil Engineering, Indian Institute of Science, Bangalore, India

²Interdisciplinary Centre for Water Research, Indian Institute of Science, Bangalore, India

Correspondence to: Pradeep P. Mujumdar (pradeep@iisc.ac.in)

Abstract. Streamflow indices are flow descriptors that quantify the streamflow dynamics, which are usually determined for a specific basin and are distinct from other basin features. The streamflow indices are appropriate for large-scale and comparative hydrology studies, independent of statistical assumptions and can distinguish signals that indicate basin behavior over time. In this paper, the characteristic features of the hydrograph's temporal asymmetry due to its different underlying hydrologic processes are primarily highlighted. Time irreversibility or temporal asymmetry refers to the steeper ascending and gradual descending parts of a streamflow hydrograph. Streamflow indices linked to each limb of the hydrograph within the time-irreversibility paradigm are distinguished with respect to its processes driving the rising and falling limbs. Various streamflow indices relating the rising and falling limbs, and the catchment attributes such as climate, topography, vegetation, geology and soil are then correlated. Finally, the key attributes governing rising and falling limbs are identified. The novelty of the work is on differentiating hydrographs by their time irreversibility property and offering an alternative way to recognize primary drivers of streamflow hydrographs. A set of streamflow indices at the catchment scale for 671 basins in the Contiguous United States (CONUS) is introduced here. These streamflow indices complement the catchment attributes provided earlier (Addor et al., 2017) for the CAMELS data set. A series of spatial maps describing the streamflow indices and their regional variability over the CONUS is illustrated in this study.

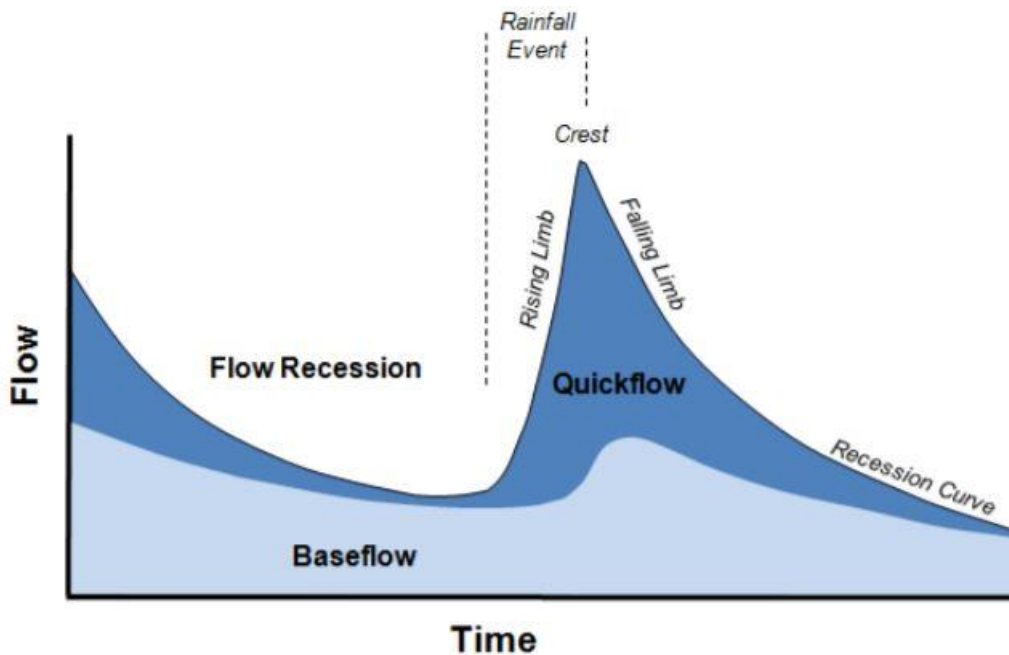
1 Introduction

Hydrologists use data to understand the hydrologic system by identifying several unique catchment signatures and employ various flow descriptors independent of statistical assumptions yet capable of capturing signals that reflect the basin's long-term unique behavior. Hydrological indices, commonly referred to as hydrologic metrics, hydrologic signatures, or diagnostic signatures, are quantitative flow metrics that characterize statistical or dynamical hydrological data series (McMillan, 2021). Specifically, streamflow indices are flow descriptors derived from discharge time-series data, and a considerable collection of indices are available to aid in the better characterization of hydrological features, ranging from basic statistics like the mean to more sophisticated metrics (Addor et al., 2018; McMillan, 2021). In many cases, daily streamflow records are not permitted for redistribution; however, researchers have computed streamflow indices and made them publicly accessible.

Hydrological indices are increasingly used in emerging areas such as global-scale hydrologic modeling and large-sample hydrology to extract relevant information and compare the different watershed processes (Addor et al., 2017, 2018; McMillan, 2021). These indices offer an indirect way to explore hydrological processes as well as

37 provide insights into hydrologic behavior in catchments where data other than streamflow is restricted and are
38 widely used in process exploration, model calibration, model selection, and catchment classification (Addor et al.,
39 2018; Clark et al., 2011; Kuentz et al., 2017; McMillan et al., 2011; Sawicz et al., 2011). McMillan (2021)
40 presented a classification that differentiates between statistics and dynamics-based signatures and between
41 signatures at different timescales.

42 The relevance of time irreversibility (or temporal asymmetry) of streamflow variability on a daily scale has been
43 emphasized in recent studies (Koutsoyiannis, 2020; Mathai and Mujumdar, 2019; Serinaldi and Kilsby, 2016).
44 The disparity in physical mechanisms driving the hydrograph's rising and falling limbs (Fig.1) contributes to time
45 irreversibility. Unlike other variables such as temperature, wind, precipitation, time irreversibility has been
46 **marked** for streamflow at a daily scale (Koutsoyiannis, 2020). Streamflow recessions convey valuable information
47 about the basin storage properties and aquifer characteristics (Aksoy & Bayazit, 2000). High variability
48 encountered in the recession behaviour of individual segments is always a challenge in modeling the recession
49 limb (Tallaksen, 1995). Recessions do not follow a simple form, due to their nonlinear nature (Aksoy et al., 2001).
50 Various segments of recession represent different stages in the flow process and **there is a need to differentiate**
51 **the recession to various segments and to characterize the recession rates separately**. As a result, time irreversibility
52 must be acknowledged in streamflow analysis, accounting for the distinction of the recession into different
53 segments, with a faster recession induced by high discharges caused by surface runoff and a slower recession
54 caused by baseflow (Fig.1), and the characterization of the recession rates separately (Mathai and Mujumdar,
55 2019). In this study, streamflow indices are chosen to better understand different hydrological processes by
56 recognizing the streamflow hydrograph's temporal asymmetry. The novelty in the work presented here is to
57 differentiate hydrograph limbs by their time irreversibility property and use their associated indices to provide an
58 approach to derive insights on the primary drivers of streamflow hydrographs.



59 **Figure 1.** Schematic representation of rising limb and falling limb
60 (source: Environment Southland;
61 <https://www.es.govt.nz/environment/water/groundwater/groundwater-monitoring>)
62

63 The analysis employs a collection of indices drawn from hydrograph shape diagnoses, to extract information about
64 the properties of rising and falling limbs of the hydrograph. The principle of time irreversibility is encapsulated
65 by six streamflow indices that characterize the shape of a streamflow hydrograph.

66 The goals of this study are as follows: i) to identify the key drivers of streamflow hydrograph (rising and falling
67 limbs) in terms of catchment attributes (eg. mean slope, aridity, fraction of precipitation falling as snow) using
68 time-irreversibility-based indices ii) to present a spatial map-based attribute class based on streamflow indices for
69 a large-sample hydrology dataset. The attribute class is a broad classification of attributes based on a particular
70 aspect/feature. *Topography, climate, and soil* are examples of attribute classes. In this study, we present a new
71 attribute class of streamflow indices related to rising and falling limbs, referred to as “*TI-streamflow indices*”
72 (*Time-irreversibility streamflow indices*).

73 Hydrograph analysis is referred to as the investigation of the numerous factors that influence hydrograph shape
74 (Rogers, 1972). The presence of hydrographs with a similar shape in long-term observation series of runoff
75 demonstrates that the same conditions of runoff generation reoccur from time to time in the catchment of a river
76 due to climate cyclicity and as a result of hydrological processes (Khrystyuk et al., 2017). Because climatic factors
77 are dynamic in space and time, they seem to be the most significant factors influencing the hydrograph shape
78 (Khrystyuk et al., 2017). Temperature, snow water equivalent, and snowmelt conditions are the most critical
79 factors influencing the shape of hydrographs (Khrystyuk et al., 2017). The shape, timing, and peak flow of a
80 streamflow hydrograph are influenced spatially and temporally by rainfall and watershed factors (Singh, 1997).
81 Using a physical laboratory model, a study has investigated the influence of chosen meteorological and
82 physiographic parameters on the runoff hydrograph (Roberts and Klingeman, 1970). Storm-related parameters
83 (rainfall intensity, rainfall duration, storm movement) and basin surface conditions are among the inputs that could
84 be experimentally modified in the model (simulated permeability, antecedent moisture conditions). The study
85 revealed that each variable was shown to have a substantial impact on the shape of the hydrograph (Roberts and
86 Klingeman, 1970). Certain factors had a more considerable impact on the rising limb of the runoff hydrograph,
87 whereas others were more important in terms of the flood crest (Roberts and Klingeman, 1970).

88 As shown in numerous studies in the literature, our notion of time-irreversibility and its indices could also perform
89 a reasonable job of articulating the catchment drivers of streamflow hydrographs. This study presents an attribute
90 class of hydrograph shape descriptors with temporal asymmetry. The significance of large-sample hydrology
91 datasets in open hydrologic science and their potential to improve hydrological studies' transparency is also
92 underlined in this study.

93 Large-sample hydrology (LSH) gathers information from a large number of catchments to gain a more
94 comprehensive understanding of hydrological processes and to go beyond individual case studies. LSH helps
95 identify catchment behavior and leads one to derive precise conclusions regarding different hydrological
96 processes and models (Addor et al., 2020). Studies involving large-sample catchments help in understanding the
97 drivers of hydrological change (Blöschl et al., 2019), in assessing hydrological similarity and classification
98 (Berghuijs et al., 2014; K. A. Sawicz et al., 2014), in predictions in ungauged basins (Ehret et al., 2014), and in
99 analysing model and data uncertainty (Coxon et al., 2014) and foster hydrology research by standardizing and
100 automating the creation of large-sample hydrology datasets worldwide (Addor et al., 2020). LSH assists in
101 exploring interrelationships between numerous catchment attributes related to landscape, climate, and hydrology

102 (Addor et al., 2017; Alvarez-Garreton et al., 2018; Gupta et al., 2014; Newman et al., 2015; Sawicz et al., 2011)
103 and generalizing rules that can significantly improve the predictability of the water cycle (Alvarez-Garreton et al.,
104 2018).

105 The primary challenges in fostering LSH are data availability and accessibility, which seriously hinder its use in
106 data-scarce regions. Despite the fact that a few large-scale hydrology studies have been undertaken, the number
107 of publicly available large-scale datasets is still restricted (Addor et al., 2017, 2020; Coxon et al., 2020). Moreover,
108 licensing restrictions and strict access policies make the datasets rarely available to the public (Coxon et al., 2020).

109 Model Parameter Estimation Experiment project (MOPEX) dataset (Duan et al., 2006), Canadian model parameter
110 experiment (CANOPEX) database (Arsenault et al., 2016), Global Streamflow Indices and Metadata Archive (Do
111 et al., 2018; Gudmundsson et al., 2018), Global Runoff Reconstruction (Ghiggi et al., 2019), HydroATLAS (Linke
112 et al., 2019) and the Catchment Attributes and MEteorology for Large-Sample studies (CAMELS) (Addor et al.,
113 2017) are notable contributions of open and accessible large-sample catchment datasets (Coxon et al., 2020). The
114 concept of time irreversibility-based streamflow indices is then applied to CAMELS catchments with the goal of
115 encouraging large-sample hydrology studies.

116 2 Methods

117 To facilitate a comprehension of various hydrological processes and streamflow hydrograph drivers, the study
118 employs streamflow indices considering the streamflow hydrograph's temporal asymmetry. The description of
119 indices used in this study are tabulated in Table 1. Streamflow indices linked to each limb of the streamflow
120 hydrograph within the time-irreversibility paradigm are distinguished since hydrographs have rising and falling
121 limbs. The following indices are considered in the rising limb category: 1) rising limb density, 2) rising limb shape
122 parameter, and 3) rising limb scale parameter. In contrast, 1) falling limb density 2) slope of upper recession
123 (upper recession coefficient) 3) slope of lower recession (lower recession coefficient) are selected in falling limb
124 category. The next step is to compute these indices for a large number of catchments and correlate them with
125 attributes such as climate, topography, vegetation, geology, and soil. The streamflow indices can be correlated
126 explicitly since sub-categories are involved in each of the catchment attributes discussed above. Finally, the key
127 attributes governing rising and falling limbs can be summarized and identified. The specifics of indices are
128 explained further below.

129 Rising limb density (RLD) is defined as the ratio of the number of rising limbs and the cumulative time of rising
130 limbs (Shamir et al., 2005). RLD is a hydrograph shape descriptor without considering the flow magnitude (Fig.
131 2) and the expression for RLD is given as,

$$132 \text{ RLD} = \frac{N_{\text{RL}}}{T_{\text{R}}} \quad (1)$$

133 The ratio of the number of falling limbs to the cumulative time of falling limbs is termed as falling limb density
(FLD) (Fig. 2) (Shamir et al., 2005). The expression for FLD is given as,

$$134 \text{ FLD} = \frac{N_{\text{FL}}}{T_{\text{F}}} \quad (2)$$

135 **Table 1.** Hydrological descriptors with temporal asymmetry.

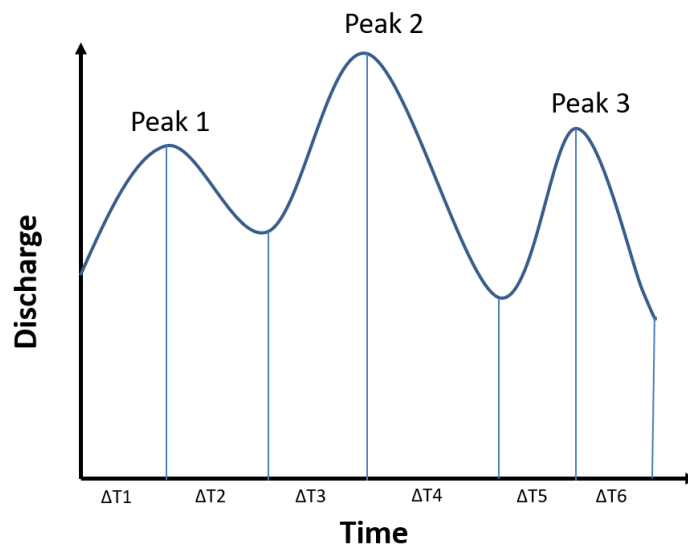
136

Attribute		Description	Unit	Data source	References
Rising limb	RLD	Rising limb density	day ⁻¹	N15 – USGS data	Shamir et al. (2005)
	a	Rising limb scale parameter	-		Mathai and Mujumdar, (2019)
	b	Rising limb shape parameter	-		Mathai and Mujumdar, (2019)
Falling limb	FLD	Falling limb density	day ⁻¹		Shamir et al. (2005)
	b ₁	Upper recession coefficient	-		Mathai and Mujumdar, (2019)
	b ₂	Lower recession coefficient	-		Mathai and Mujumdar, (2019)

137

$$\text{Rising limb density} = \frac{3}{\Delta T1 + \Delta T3 + \Delta T5}$$

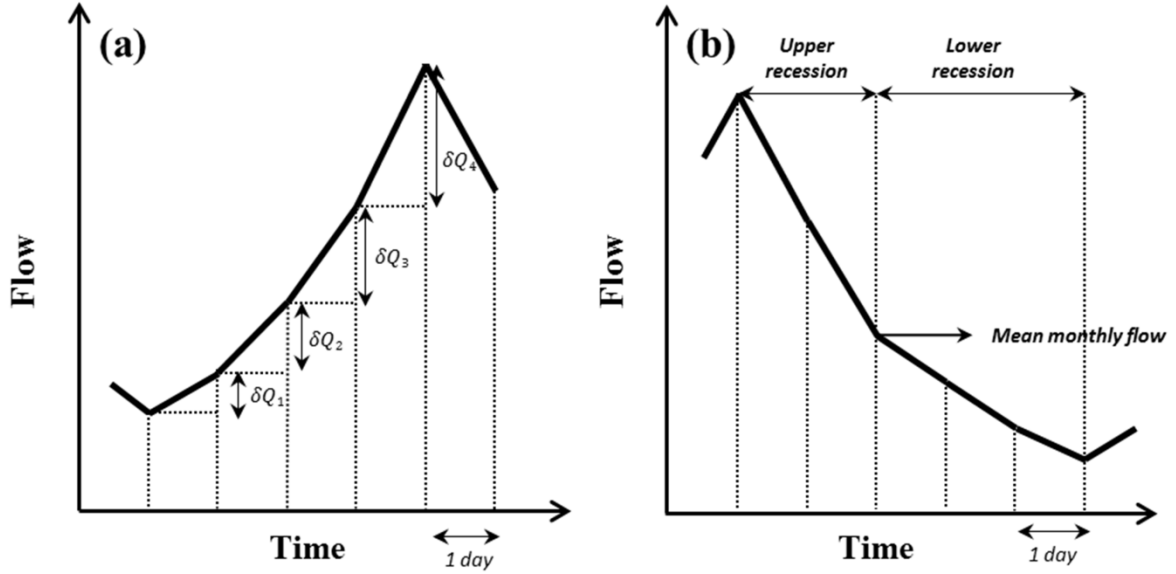
$$\text{Falling limb density} = \frac{3}{\Delta T2 + \Delta T4 + \Delta T6}$$



138

139 **Figure 2.** Schematic example of rising limb density (RLD) and falling limb density (FLD) calculation (Shamir et
140 al., 2005).

141 We first identify the hydrologic state of the stream (ascension and recession) (Mathai and Mujumdar, 2019). To
142 determine the hydrologic state of a stream - increasing (wet) or decreasing (dry) - on a given day, a time series of
143 diurnal increments is extracted by differencing the original time series with its one-day lagged time series. The
144 positive increments are identified as diurnal increments for wet days (ascension limb).



145

146 **Figure 3.** Schematic representation of flow series (a) ascension limb and (b) recession limb (Mathai and
 147 Mujumdar, 2019).

148 To characterize the shape of the rising limbs occurring on wet days, the diurnal increments are fitted using an
 149 appropriate probability density function. The Weibull distribution reflects the diurnal increments of streamflow
 150 that occur on wet days satisfactorily (Mathai and Mujumdar, 2019; Stagge and Moglen, 2013; Szilagyi et al.,
 151 2006), and the scale ' a ' and shape ' b ' parameters of the Weibull distribution are computed for each catchment by
 152 using observed diurnal increments of streamflow (indicating δQ) of the ascension limb (Fig 3.a). The Weibull pdf
 153 is positive only for positive values of x , and is zero otherwise. For strictly positive values of the scale parameter
 154 a and shape parameter b , the density function is given by

$$f(x; a, b) = \begin{cases} \frac{b}{a} \left(\frac{x}{a}\right)^{b-1} e^{-(x/a)^b} & x \geq 0, \\ 0 & x < 0, \end{cases} \quad (3)$$

155 where $a > 0$, $b > 0$. The shape and scale parameters of the Weibull distribution are estimated for each catchment
 156 from the observed diurnal increments of the streamflow. The scale parameter controls the magnitude of the
 157 increasing limb, whilst the shape parameter reflects the flashiness of the increasing limb. The scale parameter is
 158 related to the magnitude of storm events which mirrors the general shape of flows in the stream. As a result,
 159 correlating these parameters with catchment attributes reveals which catchment attributes drive the magnitude and
 160 flashiness of rising limbs.

161 In contrast, an exponential recession is used to capture the shape of the falling limbs on dry days of the daily
 162 hydrograph, representing the falling limbs' underlying dynamics (Mathai and Mujumdar, 2019). As the upper
 163 recession refers to the fast flow following a storm event and the lower recession refers to the baseflow recession,
 164 falling limb modeling is done in two stages (Fig 3.b) (Aksoy, 2003; Aksoy and Bayazit, 2000). The steps to obtain
 165 recession coefficients b_1 and b_2 are explained below (Mathai and Mujumdar, 2019). To portray the shape of the
 166 recession limbs occurring on dry days of the daily hydrograph, an exponential recession is employed to capture
 167 the falling limbs' underlying dynamics (Mathai & Mujumdar, 2019). The expression for the exponential recession
 168 is given as follows,

$$Q_t = Q_0 e^{-bt} \quad (4)$$

169 where b is the recession coefficient, t is time, Q_t is the flow t days after the peak and Q_0 is the peak flow (Mathai
 170 & Mujumdar, 2019). Mean flow value is chosen as an appropriate measure (Sargent, 1979) to divide the recession
 171 into two stages. The limbs with a peak flow value greater than the observed mean flow value are considered as
 172 upper recessions and those with peak flow values smaller than the observed mean as lower recessions. The upper
 173 recession is modelled as follows,

$$Q_t = Q_0 e^{-b_1 t} \quad (5)$$

174 where b_1 is the recession coefficient for the upper part of the recession limb, t is the number of days after the
 175 peak, Q_t is flow t days after the peak, Q_0 is the preceding peak flow (Mathai & Mujumdar, 2019). The lower
 176 recession is represented as,

$$Q_t = Q_0^* e^{-b_2(t-t^*)} \quad (6)$$

177 where b_2 is the recession coefficient for the lower part of the recession limb, t^* is the time from the start of the
 178 lower recession, Q_0^* is the initial flow in the lower part of the recession (Mathai & Mujumdar, 2019). The recession
 179 expressions for upper and lower recession are fitted by regressing $\ln(Q_t/Q_0)$ versus t and $\ln(Q_t/Q_0^*)$ versus $t -$
 180 t^* respectively. These linear regressions are performed on each individual recession sequence. The average of the
 181 upper/lower recession parameters is taken as the upper/lower recession parameter of that catchment (on daily time
 182 series data).

183 The study uses indices related to rising limb (viz., RLD, rising limb scale parameter, rising limb shape parameter)
 184 and recession limb (viz., FLD, upper recession coefficient, lower recession coefficient) to summarize the
 185 characteristic shape of steeper rising and gradually declining falling limb and its application in understanding the
 186 role of various drivers of catchment attributes in streamflow generation.

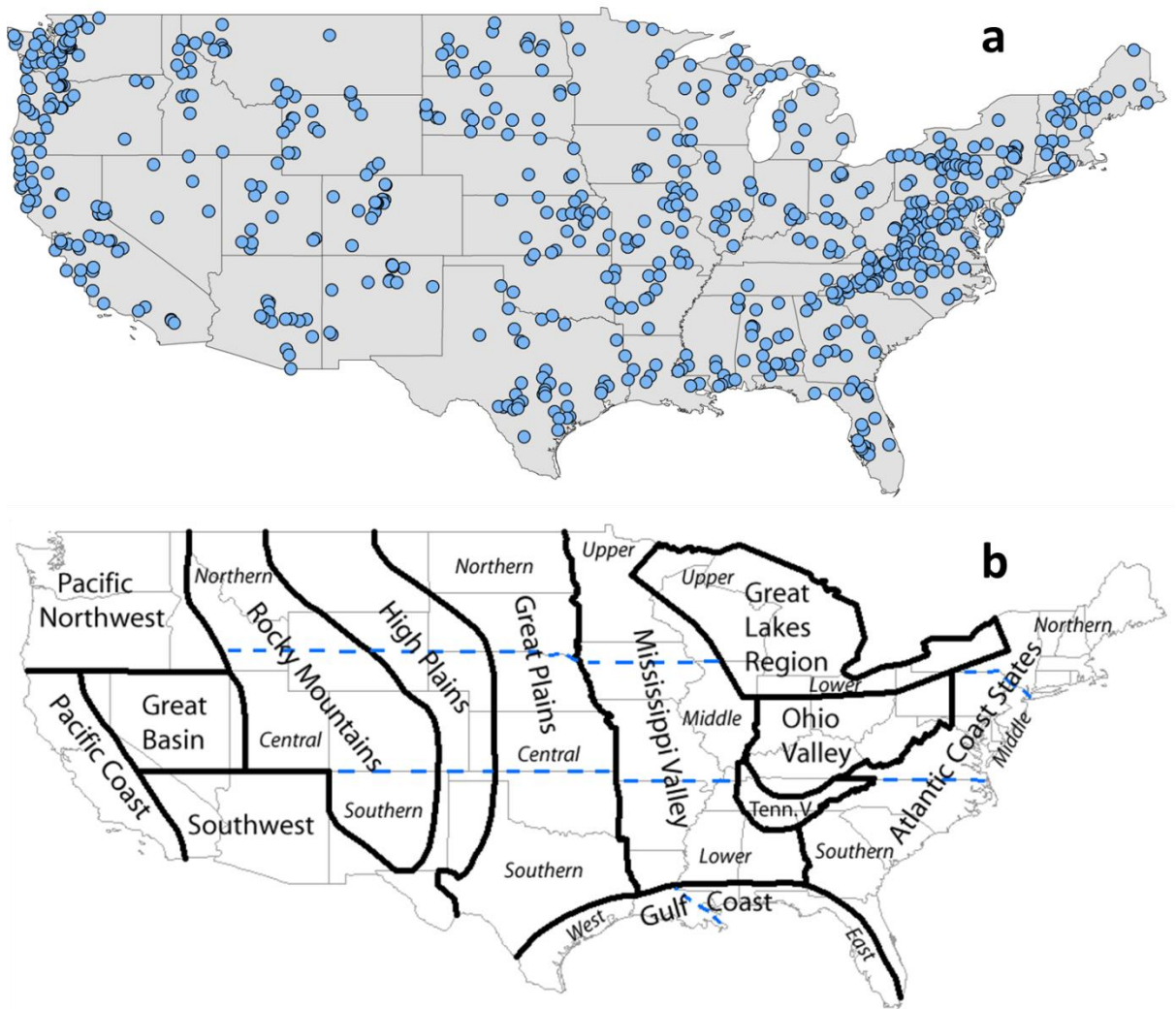
187 **3 Dataset used**

188 Section 3 provides the description of the dataset used and the study area chosen. This study employs the CAMELS
 189 dataset, which encompasses daily discharge data and catchment attributes for 671 catchments (Fig. 4) across the
 190 continental United States, representing a diverse set of catchments with long streamflow time series covering a
 191 wide range of hydro-climatic conditions (Addor et al., 2017). The time frame chosen for the analysis is from 1
 192 October 1989 to 30 September 2009 (Addor et al., 2017).

193 The topographic characteristics of CAMELS dataset are represented in Fig. S1. Except for the Appalachian
 194 Mountains, the eastern part of the Continental United States is much flatter than the western portion, according to
 195 mean elevation and mean slope maps (Fig. S1.a and S1.b). Figure S1.c depicts the spatial pattern of catchment
 196 size, highlighting presence of some catchments with an area greater than 10,000 km². The landscape of each
 197 catchment is described using multiple attributes, which can be divided into various classes as shown in Table S1
 198 (Addor et al., 2017).

199

200
201



202

203 **Figure 4.** (a) Map of 671 CAMELS catchments in the continental United States considered in this study. (b)
204 Geographical regions of US according to NOAA National Centers for Environmental Information referred for the
205 analysis (source: NOAA National Centers for Environmental Information; [https://www.ncdc.noaa.gov/temp-and-](https://www.ncdc.noaa.gov/temp-and-precip/drought/nadm/geography)
206 [precip/drought/nadm/geography](https://www.ncdc.noaa.gov/temp-and-precip/drought/nadm/geography)).

207

208

209 **4 Results and Discussion**

210 The first sub-section below looks at the regional variability of the streamflow indices used in this study. For the
211 671 CAMELS catchments, rising limb density, falling limb density, rising limb scale parameter, rising limb shape
212 parameter, upper recession coefficient, and lower recession coefficient are computed and given as spatial maps.
213 Streamflow indices are then presented in hydrological clusters to incorporate a more explicit spatial representation
214 of catchment behavior across the CONUS. Catchment attributes cover a broad range of aspects of catchment
215 hydrology such as: land cover, soil, climate, geology, topography and the association between these attributes and
216 streamflow indices is discussed further in the subsequent section. **As the climate is the most important factor in**

217 the US for the hydrological behavior for the CAMELS dataset (Jehn et al., 2020), the effect of climatic attributes
218 on streamflow indices associated with rising and falling limbs is also investigated here.

219 4.1 Spatial Variability in Streamflow Indices

220 Streamflow indices related to rising limbs and falling limbs are computed for the selected catchments and
221 displayed in spatial maps as shown in Fig. 5 and Fig. 6, respectively. The spatial analysis is based on the United
222 States' geographical areas (for details, refer to Fig. 3b) as defined by NOAA's National Centers for Environmental
223 Information and is referred to in the following spatial maps. Furthermore, ten clusters provided by Jehn et al.
224 (2020) to represent the discrete hydrological behaviors of the continental United States are adopted in this study
225 to understand the regional variability of catchment behavior. Figure S2 and Table S2 present the location map and
226 details of the ten clusters.

227 Features of the 10 clusters provided by Jehn et al. (2020) are used to interpret the findings of the results. Even
228 though a comprehensive dataset like CAMELS provides an excellent overview of various catchments in
229 contrasting climatic and topographic regions, it does not give conclusions to explain hydrologic behavior. In order
230 to address this difficulty, we transformed the streamflow indices and presented them in clusters that represent
231 distinct hydrological behavior which facilitates a ready interpretation of hydrological processes. The ten clusters
232 represent groups of catchments with distinct hydrological behavior and have distinct spatial patterns as well. The
233 clusters presented by Jehn et al. (2020) are formed based on agglomerative hierarchical clustering with ward
234 linkage on the principal components of the hydrological signatures. The hydrological signatures that are identified
235 with the highest spatial predictability are used to cluster 643 catchments from the CAMELS dataset.

236 We first identify the regions in the United States where high/low values of streamflow indices occur. The dominant
237 catchment attributes of these regions are also identified using corresponding clusters. The streamflow indices and
238 the dominant catchment attribute are then related to interpret the process behind the obtained findings. In terms
239 of geographical regions, the rising limb density is highest over the Atlantic coast states, Ohio valley, Lower
240 Mississippi Valley, Southern Great Plains, Southwest and Pacific, and lowest along the Upper Great Lakes region,
241 Upper Mississippi Valley, Great Basin, and Northern Rocky Mountains, Northern Interior Plains, and East of Gulf
242 Coast (Fig. 5.a). Further, in terms of hydrological clusters, Appalachian Mountains (Cluster 10), Southeastern and
243 Central Plains (Cluster 1) and all Southern most states of the US (Cluster 9) witness high rising limb densities and
244 these clusters are characterized by a high forest fraction, low aridity, and high frequency of high precipitation
245 events (Jehn et al., 2020), respectively (Fig. 6.a). The higher the forest proportion, the more precipitation is
246 intercepted, resulting in a shallow rising limb and longer lag time of hydrograph. A high frequency of high
247 precipitation episodes, on the other hand, can result in more rising limbs and higher rising limb densities.

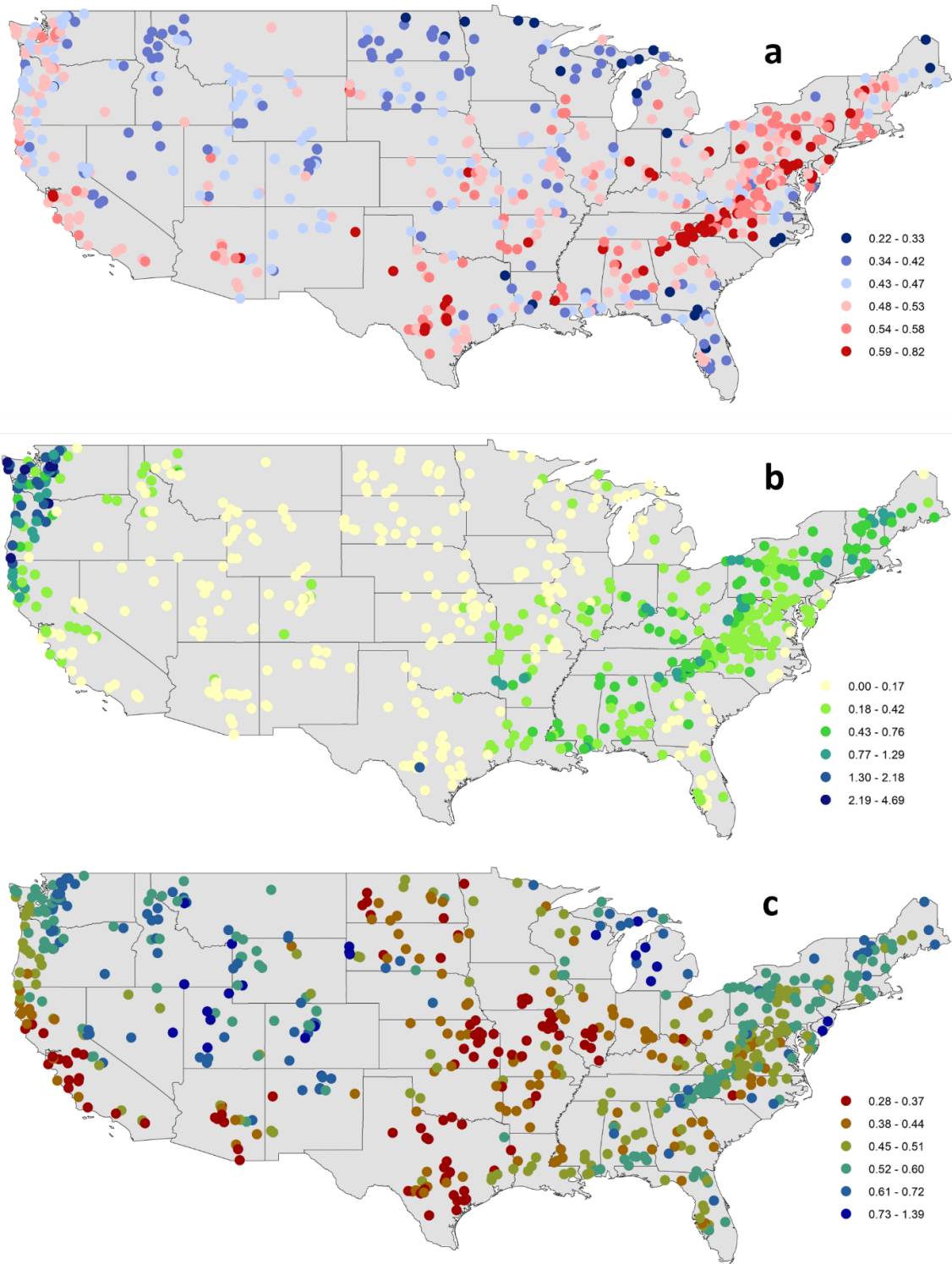
248 **Northwestern** Forested Mountains (Clusters 3, 4), located in the mountains of the western US, experience low
249 values of rising limb density as these clusters are characterized by a dominant summer peak of discharge caused
250 by rapid snowmelt (Fig. 6.a). In these clusters, we identified regions with low rising limb densities and the main
251 catchment characteristics as dominant summer discharge peaks induced by quick snowmelt (Jehn et al., 2020). A
252 long lag time and shallow rising limb might be caused by snow on the ground; hence low values of rising limbs
253 might be caused by a longer lag time.

254 Considerably low values of rising limb scale parameters are experienced over the Rocky Mountains, High Plains,
255 Great Plains, Upper Mississippi Valley, Great Basin, Southwest, and the Great Lakes regions, whereas the Pacific
256 Northwest shows high values of rising limb scale parameters (Fig. 5.b). Clusters (5, 7) over the Northwestern
257 Forested Mountains of CONUS experience very high values of rising limb scale parameters (Fig. 6.b). These
258 catchments have the highest discharge, especially in the early summer, due to a combination of high precipitation
259 and snowmelt. Further, the region in the Continental US which receives the highest precipitation is included in
260 Cluster 5. Moreover, Cluster 5 consists of a large proportion of forest. Again, Cluster 7 with high values of rising
261 limb scale parameter is characterized by high fraction of precipitation falling as snow. High precipitation and
262 snowmelt might result in a large discharge. Higher discharges can create higher values of rising scale parameters
263 as the rising limb scale parameter regulates the magnitude of the rising limb. Low values of rising limb scale
264 parameters are shown by Clusters 2, 8, 9. This is because of low water availability, low snow fraction precipitation
265 falling as snow, and high evaporation experienced in these regions. Low discharge and thus lower rising limb
266 scale parameters can be caused by excessive evaporation, low water availability, and a low snow fraction of
267 precipitation falling as snow.

268 Low rising limb shape parameter occurs along the Great Plains, Mississippi Valley, Pacific coast, and the west of
269 Gulf Coast (Fig. 5.c). In contrast, the shape parameter over the Rocky Mountains, High Plains, Great Basin, Pacific
270 Northwest, and the Great Lakes region witnesses the highest values of rising limb shape parameters (Fig. 5.c). All
271 the catchments located in the Southern states of the US (Cluster 9), Great Plains and North American deserts
272 (Cluster 8), and the Central Plains (Cluster 2) characterize low values of rising limb shape parameters (Fig. 6.c).
273 This is due to low water availability, low snow fraction precipitation falling as snow, low leaf area index, and high
274 evaporation experienced in these regions. Excessive evaporation and a low snow fraction of precipitation falling
275 as snow can contribute to low discharge and thus lower rising limb shape parameters. High values of rising limb
276 shape parameters are seen in Clusters 3, 4 (Fig. 6.c) located in the Northwestern Forested Mountains of the western
277 US, dominant with a summer peak of discharge caused by rapid snowmelt. The rapid snowmelt can cause flashy
278 hydrographs with high values of rising limb shape parameters.

279 Catchments with a high falling limb density are predominantly located along the Great Basin and the Rocky
280 Mountains and in the High Plains region (Fig. 7.a). Clusters 4, 2, 8 over Northwestern Forested Mountains, Central
281 Plains, Great Plains, and North American deserts characterize higher magnitudes of falling limb density, and
282 Clusters 6, 7 over Marine West Coast Forests and Western Cordillera smaller falling limb densities (Fig. 8.a).
283 This is due to less presence of forest cover in these arid regions and falling limb density shows a positive
284 association with the arid climate.

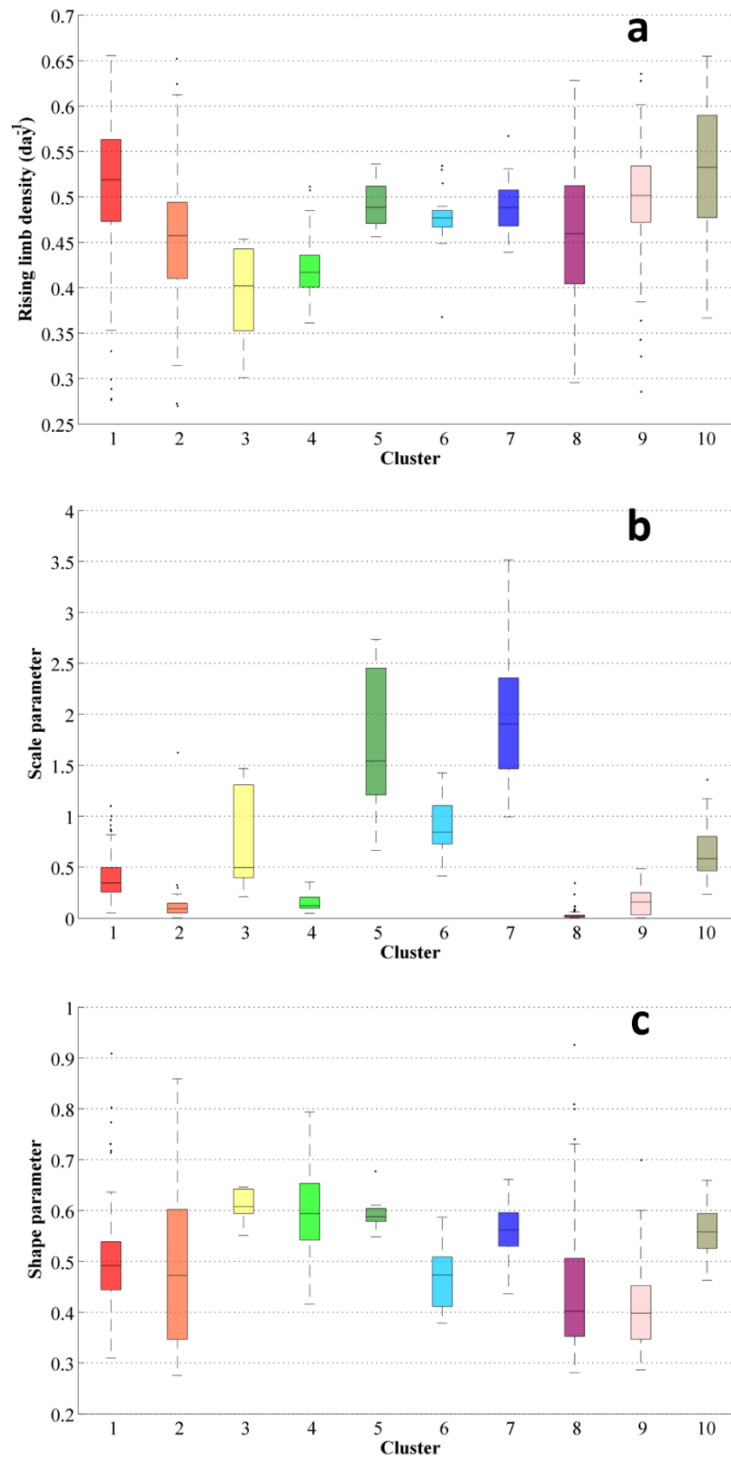
285 Similarities exist between the patterns of the upper recession coefficient and the lower recession coefficient (Fig.
286 7.b and Fig. 7.c). Clusters 3, 4 located in the Northwestern Forested Mountains, which have overall low discharge,
287 show low values of upper and lower recession coefficients (Fig. 8.b and Fig. 8.c). Clusters 2 and 9, located in the
288 eastern US, witness high values of recession coefficients; due to low slope inclinations, water takes a long time
289 to reach the outlet (Fig. 8.b and Fig. 8.c).



290

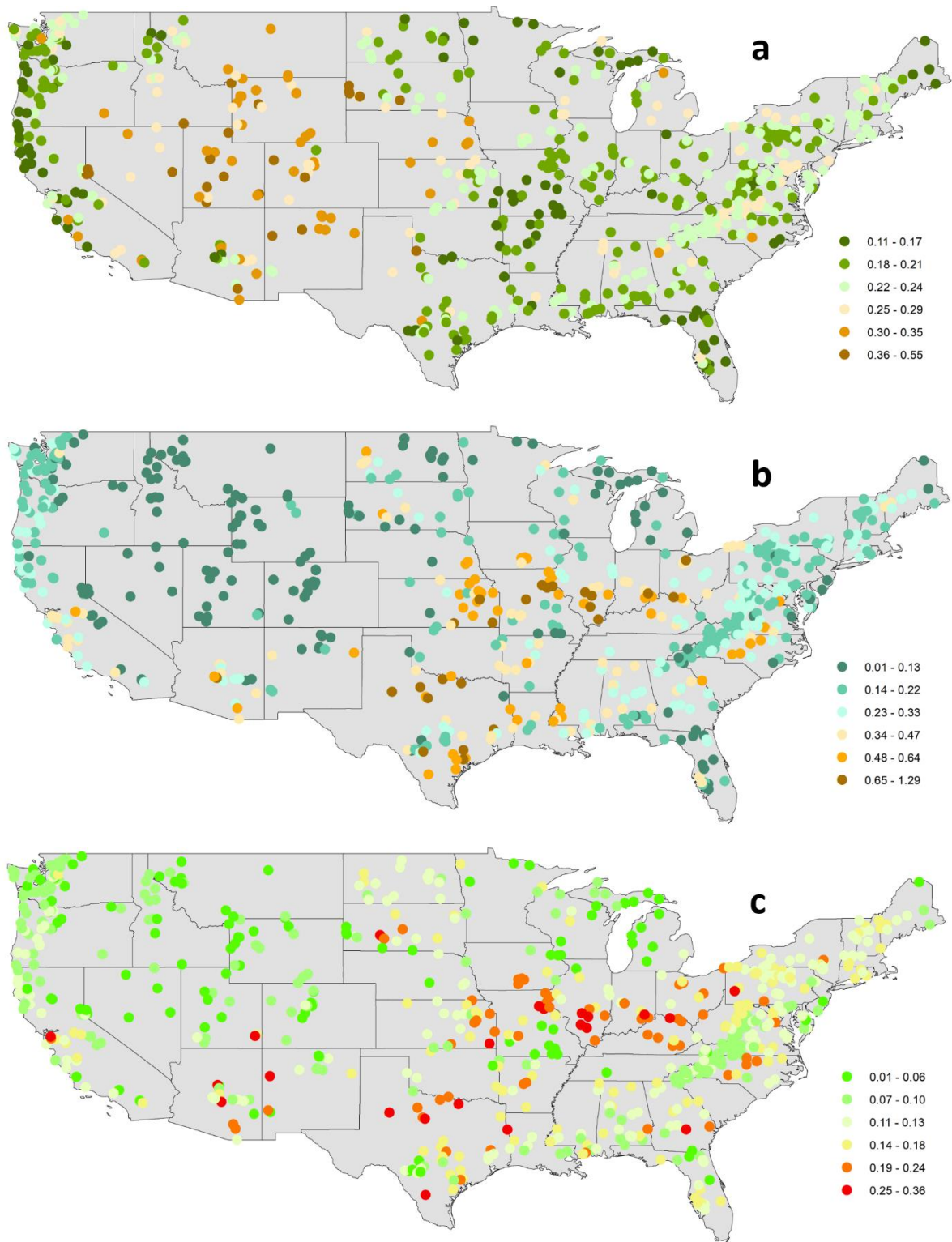
291 **Figure 5.** Spatial maps of streamflow indices associated with a rising limb (a) rising limb density [day^{-1}], (b)
 292 rising limb scale parameter, (c) rising limb shape parameter over the CONUS.

293



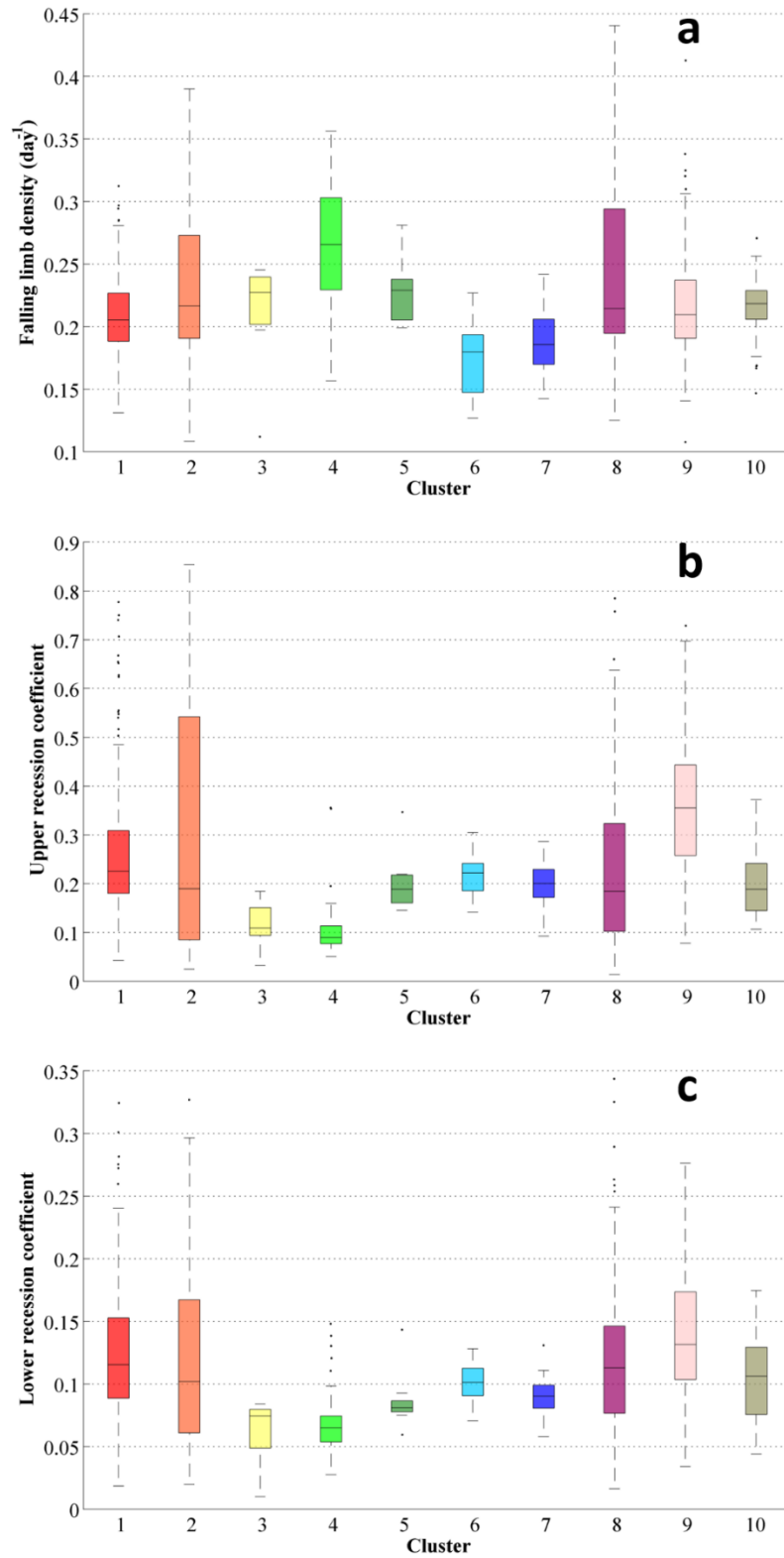
294

295 **Figure 6.** Boxplots of the hydrological descriptors linked with the rising limb (a) rising limb density [day^{-1}], (b)
 296 rising limb scale parameter, (c) rising limb shape parameter of the clusters over the CONUS.



297

298 **Figure 7.** Regional variability of streamflow indices associated with the falling limb (a) falling limb density [day^{-1}], (b) upper recession coefficient, (c) lower recession coefficient over the CONUS.
 299



300

301 **Figure 8.** Boxplots of the streamflow indices related with the falling limb (a) falling limb density [day⁻¹], (b)
 302 upper recession coefficient, (c) lower recession coefficient of the clusters.

303

304 4.2 Relation of the Streamflow Indices and the Catchment Attributes

305 The association between the streamflow indices related to rising and falling limbs and catchment attributes is
306 examined in this section. Table 2 shows the relation of streamflow indices linked with rising limb, and Table 3
307 shows the association of indices of the falling limb with catchment attributes. We used Spearman rank correlation
308 for the correlation analysis. (in Tables 2 and 3). Green-colored coefficients represent positive correlation, and the
309 red-colored correlation coefficients represent negative correlation. Table 2 and Table 3 have certain columns that
310 are blank because only significant correlation values are provided in the table. Across all five attribute classes, the
311 vegetation/land cover attributes positively correlate with all rising limb indices (Table 2). It can be seen that the
312 rising limb density shows a positive correlation with all the three vegetation density indicators, namely fraction
313 of forest, maximum leaf area index, maximum green vegetation fraction (Table 2).

314
315 However, it is observed that the rising limb scale parameter shows a negative correlation with climate and a
316 positive association with the vegetation attributes (Table 2). Aridity and frequency of precipitation (Table 2)
317 display a strong negative association with the rising limb scale parameter. It is noted that the rising limb shape
318 parameter indicates a positive correlation with vegetation attributes and the fraction of precipitation falling as
319 snow, mean slope, mean elevation, and sand fraction whereas, it negatively correlates with precipitation
320 frequency.

321
322 Falling limb density is mainly governed by climate indices and is negatively correlated with the land cover
323 characteristics (Table 3). Mean elevation also strongly characterizes the nature of the falling limb density. Besides,
324 aridity and fraction of precipitation falling as snow are also positively correlated with falling limb density.
325 Recession coefficients are negatively correlated with topographic indices (Table 3). Further, the recession
326 coefficients show a positive correlation with clay and negative correlations with the fraction of precipitation falling
327 as snow, forest fraction, and sand fraction. Moreover, the geology attributes such as subsurface porosity reveal a
328 positive correlation to recession coefficients and a negative with subsurface permeability (Table 3).

329

330

331

332 **Table 2.** Correlation between streamflow indices linked with rising limb and the catchment attributes. Green
 333 colored coefficients represent positive correlation, and the red-colored correlation coefficients represent the
 334 negative correlation.

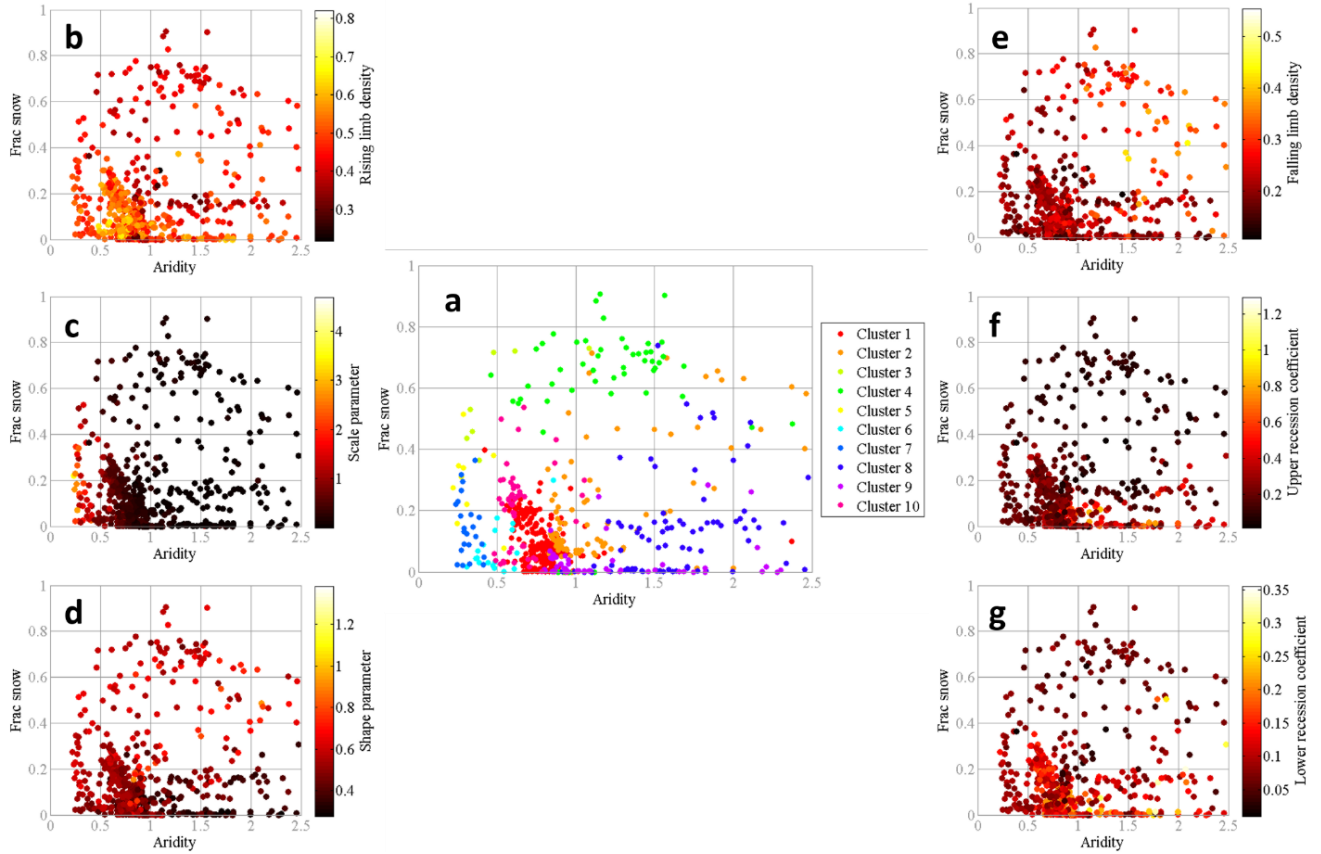
Spearman rank correlation coefficients	Topography			Climate						Soil			Land cover			Geology		
	Area	Mean elevation	Mean slope	Precipitation seasonality	Frac of precp as snow	Aridity	High precp freq	High precp dur	Low precp freq	Low precp dur	Depth to bedrock	Sand frac	Clay frac	Forest frac	LAI maximum	Green veg frac max	Subsurface porosity	Subsurface permeability
Rising limb density	-0.30	-0.20			-0.33	-0.10	0.08	-0.15			-0.32	-0.28	0.26	0.10	0.20	0.18	-0.16	-0.11
Scale parameter	-0.17	-0.13	0.35	-0.36		-0.53	-0.56		-0.63	-0.25	-0.21		-0.15	0.46	0.41	0.44		
Shape parameter		0.41	0.36	-0.14	0.53	-0.16	-0.42		-0.45	-0.29	-0.16	0.37	-0.47	0.41	0.17	0.15	-0.16	

335 **Table 3.** Correlation between streamflow indices linked with falling limb and the catchment attributes. Green
 336 colored coefficients represent positive correlation, and the red-colored correlation coefficients represent the
 337 negative correlation.

338

Spearman rank correlation coefficients	Topography			Climate						Soil			Land cover			Geology		
	Area	Mean elevation	Mean slope	Precipitation seasonality	Frac of precp as snow	Aridity	High precp freq	High precp dur	Low precp freq	Low precp dur	Depth to bedrock	Sand frac	Clay frac	Forest frac	LAI maximum	Green veg frac max	Subsurface porosity	Subsurface permeability
Falling limb density	-0.13	0.55	0.18		0.42	0.39	0.12	0.12	0.17	0.11	-0.19			-0.17	-0.37	-0.40	0.08	
Upper recession coefficient		-0.40	-0.38	0.17	-0.46		0.31	-0.11	0.26		0.19	-0.38	0.52	-0.31	-0.09		0.13	-0.09
Lower recession coefficient		-0.35	-0.37	0.22	-0.39		0.27	-0.17	0.19		0.21	-0.23	0.32	-0.28			0.16	-0.18

339



340

341 **Figure 9.** (a) Comparison of the hydrological clusters of Jehn et al. (2020) with the climate index space (fraction
 342 of precipitation falling as snow vs. aridity). Single dots show the catchments and are colored by their hydrological
 343 clusters. Comparison of the streamflow indices in climate index space (b) rising limb density (c) rising limb scale
 344 parameter, (d) rising limb shape parameter, (e) falling limb density, (f) upper recession coefficient, (g) lower
 345 recession coefficient for all catchments. Single dots show the catchments and are colored according to the value
 346 of the streamflow indices.

347

348 4.3 Influence of Attributes of Climate to Streamflow Indices

349 The climatic indices indicate a more substantial influence on hydrological signatures than the topographic, soil,
 350 land cover, and geological attributes combined (Addor et al., 2018). Additionally, the findings of Jehn et al. (2020)
 351 highlighted that the climate appears to be the most critical factor influencing hydrological behavior in the
 352 CAMELS dataset as a whole, and depending on the location, either aridity, snow, or seasonality are most
 353 important. Hence, the streamflow indices are then examined in the climate index space (aridity along x-axis and
 354 fraction of precipitation falling as snow along the y-axis) to evaluate the main drivers of the catchments. Single
 355 dots show the catchments and are colored by their hydrological clusters (Fig. 9.a).

356 Clusters 5, 6, 7, 1, 10 are characterized by a low fraction of precipitation falling as snow and humid climate,
 357 whereas Clusters 3, 4 have humid climate experiencing a high fraction of precipitation falling as snow (Fig. 9.a).
 358 Clusters 2, 8, 9 are featured by a low fraction of precipitation falling as snow and arid climate (Fig. 9.a). The three
 359 categories mentioned above are referred to as G1, G2, and G3, respectively.

360 Clusters G1 with a low fraction of precipitation falling as snow with humid climate show (Clusters 1, 9, 10) high
361 rising limb densities (Fig. 9.b) and (Clusters 5, 7) high rising limb scale parameters (Fig. 9.c). This is because the
362 rising limb density negatively correlates with fraction of precipitation falling as snow (Fig. 9.b), whereas the rising
363 limb scale parameter negatively correlates with aridity (Fig. 9.c). Moreover, these Clusters G1 experience a low
364 value of (Clusters 6, 7) falling limb density (Fig. 9.e). This is because the falling limb density positively correlates
365 with the climate indices (Fig. 9.e).

366 As mentioned earlier, Clusters G2 with humid climate and with a high fraction of precipitation falling as snow
367 (Clusters 3, 4) display low values of rising limb density as rising limb density correlates negatively with the
368 fraction of precipitation falling as snow (Fig. 9.b). G2 witnesses higher values of rising limb shape parameter due
369 to its negative correlation with aridity and positive correlation with the fraction of precipitation falling as snow
370 (Fig. 9.d). Furthermore, the Clusters of G2 (Clusters 3, 4) show low values of recession coefficients as they depict
371 a strong negative correlation with the fraction of precipitation falling as snow (Fig. 9.f, g).

372 Low values of rising limb scale and shape parameters are noticed for the Clusters 2, 9, 8 (Clusters G3) with arid
373 climate and low fraction of precipitation falling as snow (Fig. 9.c, d) due to its negative correlation with aridity as
374 stated earlier. Cluster 8 experiences the maximum values of falling limb density (Fig. 9.e) where the region
375 witnesses low fraction of snow and arid catchments, due to its strong positive correlates with the aridity.

376 5 Concluding remarks

377 Streamflow hydrograph portrays the time distribution of runoff at the point of measurement by a single curve, and
378 the hydrographs are characterized by their time irreversibility property. In this study, the indices related to this
379 characteristic feature are used to study the catchment drivers of streamflow hydrograph. The streamflow indices
380 associated with the time irreversibility of hydrograph open new opportunities to investigate the interaction
381 between topography, soil, climate, vegetation, geology that drive the hydrological behavior of catchments.
382 Moreover, most of the previously presented hydrologic indices are employed only for time-symmetric processes
383 (McMillan, 2021); the importance of the time irreversibility of streamflow is highlighted in this study. The indices
384 associated with rising and falling limbs are primarily correlated to distinct catchment attributes, establishing a
385 relationship between the indices and catchment attributes such as climate, topography, soil, geology, and
386 vegetation to delineate the controlling drivers in corresponding hydrograph sections. A set of streamflow indices
387 with temporal asymmetry for 671 catchments in the United States is presented in this study. The regional
388 variations among catchments over the United States are compared and discussed using the spatial maps of
389 streamflow indices. Such spatial maps of the streamflow indices supplement the hydrometeorological time series
390 and catchment attributes provided by Addor et al. (2017).

391 The study revealed that the rising limb indices such as rising limb density, rising limb shape parameter and rising
392 limb scale parameter correlate positively with vegetation indices. Falling limb density is primarily controlled by
393 climate indices and is negatively correlated with land cover characteristics; the structure of the falling limb density
394 is also closely influenced by mean elevation. Finally, streamflow indices are studied in the climate index space to
395 isolate the runoff generation's leading drivers. High rising limb densities and rising limb scale parameters are
396 observed in catchments with low precipitation falling as snow and a humid climate. It is observed that the
397 catchments with a humid climate and a high fraction of precipitation falling as snow display low values of rising

398 limb density, high values of the rising limb shape parameter, and low values of recession coefficients. The lowest
399 values of rising limb scale and shape parameters, and the highest values of falling limb density, are seen in
400 catchments of arid climates and a low fraction of precipitation falling as snow.

401 In general, the contribution of this work lies in differentiating hydrographs depending on their time irreversibility
402 property and using the corresponding indices to provide an alternative methodology for identifying the drivers of
403 streamflow hydrographs. In the context of largesample hydrology research, the concept of time-irreversibility and
404 the indices associated with it could also be used to describe the drivers at catchment scale.

405

406 *Data availability.* The CAMELS dataset can be found at <https://doi.org/10.5194/hess21-5293-2017> (Addor et al.
407 2017).

408 *Competing interests.* The authors declare that they have no conflict of interest.

409 *Acknowledgements.* We would like to thank all the people who created the CAMELS dataset. The funding
410 received from the Ministry of Earth Sciences (MoES), Government of India, through the project, “Advanced
411 Research in Hydrology and Knowledge Dissemination”, Project No.: MOES/PAMC/H&C/41/2013-PC-II, is
412 gratefully acknowledged.

413

414 **References**

415

416 Addor, Newman, A. J., Mizukami, N. and Clark, M. P.: The CAMELS data set: catchment attributes and
417 meteorology for large-sample studies, *Hydrol. Earth Syst. Sci.*, 21(10), 5293–5313, doi:10.5194/hess-21-5293-
418 2017, 2017.

419 Addor, Nearing, G., Prieto, C., Newman, A. J., Le Vine, N. and Clark, M. P.: A Ranking of Hydrological
420 Signatures Based on Their Predictability in Space, *Water Resour. Res.*, 54(11), 8792–8812,
421 doi:10.1029/2018WR022606, 2018.

422 Addor, N., Do, H. X., Alvarez-Garreton, C., Coxon, G., Fowler, K. and Mendoza, P. A.: Large-sample hydrology:
423 recent progress, guidelines for new datasets and grand challenges, *Hydrol. Sci. J.*, 65(5), 712–725,
424 doi:10.1080/02626667.2019.1683182, 2020.

425 Alvarez-Garreton, C., Mendoza, P. A., Pablo Boisier, J., Addor, N., Galleguillos, M., Zambrano-Bigiarini, M.,
426 Lara, A., Puelma, C., Cortes, G., Garreaud, R., McPhee, J. and Ayala, A.: The CAMELS-CL dataset: Catchment
427 attributes and meteorology for large sample studies-Chile dataset, *Hydrol. Earth Syst. Sci.*, 22(11), 5817–5846,
428 doi:10.5194/hess-22-5817-2018, 2018a.

429 Alvarez-Garreton, C., Mendoza, P. A., Boisier, J. P., Addor, N., Galleguillos, M., Zambrano-Bigiarini, M., Lara,
430 A., Puelma, C., Cortes, G., Garreaud, R., McPhee, J. and Ayala, A.: The CAMELS-CL dataset: catchment
431 attributes and meteorology for large sample studies – Chile dataset, *Hydrol. Earth Syst. Sci.*, 22(11), 5817–5846,
432 doi:10.5194/hess-22-5817-2018, 2018b.

433 Arsenault, R., Bazile, R., Ouellet Dallaire, C. and Brissette, F.: CANOPEX: A Canadian hydrometeorological
434 watershed database, *Hydrol. Process.*, 30(15), 2734–2736, doi:10.1002/hyp.10880, 2016.

435 Berghuijs, W. R., Sivapalan, M., Woods, R. A. and Savenije, H. H. G.: Patterns of similarity of seasonal water
436 balances: A window into streamflow variability over a range of time scales, *Water Resour. Res.*, 50(7), 5638–
437 5661, doi:10.1002/2014WR015692, 2014.

438 Blöschl, G., Hall, J., Viglione, A., Perdigão, R. A. P., Parajka, J., Merz, B., Lun, D., Arheimer, B., Aronica, G.
439 T., Bilibashi, A., Boháč, M., Bonacci, O., Borga, M., Čanjevac, I., Castellarin, A., Chirico, G. B., Claps, P.,
440 Frolova, N., Ganora, D., Gorbachova, L., Gül, A., Hannaford, J., Harrigan, S., Kireeva, M., Kiss, A., Kjeldsen, T.
441 R., Kohnová, S., Koskela, J. J., Ledvinka, O., Macdonald, N., Mavrova-Guirguinova, M., Mediero, L., Merz, R.,
442 Molnar, P., Montanari, A., Murphy, C., Osuch, M., Ovcharuk, V., Radevski, I., Salinas, J. L., Sauquet, E., Šraj,
443 M., Szolgay, J., Volpi, E., Wilson, D., Zaimi, K. and Živković, N.: Changing climate both increases and decreases
444 European river floods, *Nature*, 573(7772), 108–111, doi:10.1038/s41586-019-1495-6, 2019.

445 Clark, M. P., McMillan, H. K., Collins, D. B. G., Kavetski, D. and Woods, R. A.: Hydrological field data from a
446 modeller’s perspective: Part 2: Process-based evaluation of model hypotheses, *Hydrol. Process.*, 25(4), 523–543,
447 doi:10.1002/hyp.7902, 2011.

448 Coxon, G., Freer, J., Wagener, T., Odoni, N. A. and Clark, M.: Diagnostic evaluation of multiple hypotheses of
449 hydrological behaviour in a limits-of-acceptability framework for 24 UK catchments, *Hydrol. Process.*, 28(25),
450 6135–6150, doi:10.1002/hyp.10096, 2014.

451 Coxon, G., Addor, N., Bloomfield, J. P., Freer, J., Fry, M., Hannaford, J., Howden, N. J. K., Lane, R., Lewis, M.,
452 Robinson, E. L., Wagener, T. and Woods, R.: CAMELS-GB: hydrometeorological time series and landscape
453 attributes for 671 catchments in Great Britain, *Earth Syst. Sci. Data*, 12(4), 2459–2483, doi:10.5194/essd-12-
454 2459-2020, 2020.

455 Do, H. X., Gudmundsson, L., Leonard, M. and Westra, S.: The Global Streamflow Indices and Metadata Archive
456 (GSIM) – Part 1: The production of a daily streamflow archive and metadata, *Earth Syst. Sci. Data*, 10(2), 765–
457 785, doi:10.5194/essd-10-765-2018, 2018.

458 Duan, Q., Schaake, J., Andréassian, V., Franks, S., Goteti, G., Gupta, H. V., Gusev, Y. M., Habets, F., Hall, A.,
459 Hay, L., Hogue, T., Huang, M., Leavesley, G., Liang, X., Nasonova, O. N., Noilhan, J., Oudin, L., Sorooshian,
460 S., Wagener, T. and Wood, E. F.: Model Parameter Estimation Experiment (MOPEX): An overview of science
461 strategy and major results from the second and third workshops, *J. Hydrol.*, 320(1–2), 3–17,
462 doi:10.1016/j.jhydrol.2005.07.031, 2006.

463 Ehret, U., Gupta, H. V., Sivapalan, M., Weijjs, S. V., Schymanski, S. J., Blöschl, G., Gelfan, A. N., Harman, C.,
464 Kleidon, A., Bogaard, T. A., Wang, D., Wagener, T., Scherer, U., Zehe, E., Bierkens, M. F. P., Di Baldassarre,
465 G., Parajka, J., van Beek, L. P. H., van Griensven, A., Westhoff, M. C. and Winsemius, H. C.: Advancing
466 catchment hydrology to deal with predictions under change, *Hydrol. Earth Syst. Sci.*, 18(2), 649–671,
467 doi:10.5194/hess-18-649-2014, 2014.

468 Ghiggi, G., Humphrey, V., Seneviratne, S. I. and Gudmundsson, L.: GRUN: an observation-based global gridded
469 runoff dataset from 1902 to 2014, *Earth Syst. Sci. Data*, 11(4), 1655–1674, doi:10.5194/essd-11-1655-2019, 2019.

470 Gudmundsson, L., Do, H. X., Leonard, M. and Westra, S.: The Global Streamflow Indices and Metadata Archive
471 (GSIM) – Part 2: Quality control, time-series indices and homogeneity assessment, *Earth Syst. Sci. Data*, 10(2),
472 787–804, doi:10.5194/essd-10-787-2018, 2018.

473 Gupta, H. V., Perrin, C., Blöschl, G., Montanari, A., Kumar, R., Clark, M. and Andréassian, V.: Large-sample
474 hydrology: a need to balance depth with breadth, *Hydrol. Earth Syst. Sci.*, 18(2), 463–477, doi:10.5194/hess-18-
475 463-2014, 2014.

476 Jehn, F. U., Bestian, K., Breuer, L., Kraft, P. and Houska, T.: Using hydrological and climatic catchment clusters
477 to explore drivers of catchment behavior, *Hydrol. Earth Syst. Sci.*, 24(3), 1081–1100, doi:10.5194/hess-24-1081-
478 2020, 2020.

479 Khrystyuk, B., Gorbachova, L. and Koshkina, O.: The impact of climatic conditions of spring flood formation
480 on hydrograph shape of the Desna River, *Meteorol. Hydrol. Water Manag.*, 5(1), 63–70,
481 doi:10.26491/mhwm/67914, 2017.

482 Koutsoyiannis, D.: Simple stochastic simulation of time irreversible and reversible processes, *Hydrol. Sci. J.*,
483 doi:10.1080/02626667.2019.1705302, 2020.

484 Kuentz, A., Arheimer, B., Hundecha, Y. and Wagener, T.: Understanding hydrologic variability across Europe
485 through catchment classification, *Hydrol. Earth Syst. Sci.*, 21(6), 2863–2879, doi:10.5194/hess-21-2863-2017,
486 2017.

487 Linke, S., Lehner, B., Ouellet Dallaire, C., Ariwi, J., Grill, G., Anand, M., Beames, P., Burchard-Levine, V.,
488 Maxwell, S., Moidu, H., Tan, F. and Thieme, M.: Global hydro-environmental sub-basin and river reach
489 characteristics at high spatial resolution, *Sci. Data*, 6(1), 283, doi:10.1038/s41597-019-0300-6, 2019.

490 Mathai and Mujumdar, P. P.: Multisite Daily Streamflow Simulation With Time Irreversibility, *Water Resour.*
491 *Res.*, 55(11), 9334–9350, doi:10.1029/2019WR025058, 2019.

492 McMillan, H. K.: A review of hydrologic signatures and their applications, *WIREs Water*, 8(1), 1–23,
493 doi:10.1002/wat2.1499, 2021.

494 McMillan, H. K., Clark, M. P., Bowden, W. B., Duncan, M. and Woods, R. A.: Hydrological field data from a
495 modeller’s perspective: Part 1. Diagnostic tests for model structure, *Hydrol. Process.*, 25(4), 511–522,
496 doi:10.1002/hyp.7841, 2011.

497 Newman, A. J., Clark, M. P., Sampson, K., Wood, A., Hay, L. E., Bock, A., Viger, R. J., Blodgett, D., Brekke,
498 L., Arnold, J. R., Hopson, T. and Duan, Q.: Development of a large-sample watershed-scale hydrometeorological
499 data set for the contiguous USA: data set characteristics and assessment of regional variability in hydrologic model
500 performance, *Hydrol. Earth Syst. Sci.*, 19(1), 209–223, doi:10.5194/hess-19-209-2015, 2015.

501 Richter, B. D., Baumgartner, J. V., Powell, J. and Braun, D. P.: A Method for Assessing Hydrologic Alteration
502 within Ecosystems, *Conserv. Biol.*, 10(4), 1163–1174, doi:10.1046/j.1523-1739.1996.10041163.x, 1996.

503 Roberts, M. C. and Klingeman, P. C.: The influence of landform and precipitation parameters on flood
504 hydrographs, *J. Hydrol.*, 11(4), 393–411, doi:10.1016/0022-1694(70)90004-1, 1970.

505 Rogers, W. F.: New concept in hydrograph analysis, *Water Resour. Res.*, 8(4), 973–981,
506 doi:10.1029/WR008i004p00973, 1972.

507 Sawicz, K., Wagener, T., Sivapalan, M., Troch, P. A. and Carrillo, G.: Catchment classification : empirical
508 analysis of hydrologic similarity based on catchment function in the eastern USA, *Hydrol. Earth Syst. Sci.*, 8(3),
509 2895–2911, doi:10.5194/hess-15-2895-2011, 2011.

510 Sawicz, K. A., Kelleher, C., Wagener, T., Troch, P., Sivapalan, M. and Carrillo, G.: Characterizing hydrologic
511 change through catchment classification, *Hydrol. Earth Syst. Sci.*, 18(1), 273–285, doi:10.5194/hess-18-273-
512 2014, 2014.

513 Serinaldi, F. and Kilsby, C. G.: Irreversibility and complex network behavior of stream flow fluctuations, *Phys.*
514 *A Stat. Mech. its Appl.*, 450, 585–600, doi:10.1016/j.physa.2016.01.043, 2016.

515 Shamir, E., Imam, B., Morin, E., Gupta, H. V. and Sorooshian, S.: The role of hydrograph indices in parameter
516 estimation of rainfall-runoff models, *Hydrol. Process.*, 19(11), 2187–2207, doi:10.1002/hyp.5676, 2005.

517 Singh, V. P.: Effect of spatial and temporal variability in rainfall and watershed characteristics on stream flow
518 hydrograph, *Hydrol. Process.*, 11(12), 1649–1669, doi:10.1002/(SICI)1099-1085(19971015)11:12<1649::AID-
519 HYP495>3.0.CO;2-1, 1997.

520 Stage, J. H. and Moglen, G. E.: A nonparametric stochastic method for generating daily climate-adjusted
521 streamflows, *Water Resour. Res.*, 49, 6179–6193, doi:10.1002/wrcr.20448, 2013.

522 Szilagyi, J., Balint, G. and Csik, A.: Hybrid, Markov chain-based model for daily streamflow generation at
523 multiple catchment sites, *J. Hydrol. Eng.*, 11(3), 245–256, 2006.